Magnetic structure of $Fe_{16}N_2$ determined by polarized neutron diffraction on thin-film samples

Xudong Hang,[1] Masaaki Matsuda,[2] Jacob T. Held,[1] K. Andre Mkhoyan,[1] and Jian-Ping Wang[3,*]
[1]*Department of Chemical Engineering and Materials Science, University of Minnesota, Minneapolis, Minnesota 55455, USA*
[2]*Neutron Scattering Division, Oak Ridge National Laboratory, Oak Ridge, Tennessee 37831, USA*
[3]*Department of Electrical and Computer Engineering, University of Minnesota, Minneapolis, Minnesota 55455, USA*

(Received 6 July 2020; accepted 20 August 2020; published 2 September 2020)

Strain-free $Fe_{16}N_2$ thin films were obtained on MgO (001) single-crystal substrates with Cr seed layers. X-ray diffraction and transmission electron microscopy confirmed that the film is textured in all three spatial directions with crystallographic orientation determined by epitaxial constraints from the substrate. Average grain size was estimated to be in the range of tens of nanometers. Ten pieces of 40-nm-thick $Fe_{16}N_2$ thin-film samples were stacked together for half-polarized neutron diffraction study at room temperature. A total of six reflections were usable, from which the magnetic structure of $Fe_{16}N_2$ was determined and compared to existing models. Contrary to most electronic structure calculations, the present results suggest that the magnetic moment of Fe atoms at the 8*h* site is large and larger than that of the 4*d* site. Our results support the giant magnetization of $Fe_{16}N_2$.

DOI: 10.1103/PhysRevB.102.104402

I. INTRODUCTION

High-magnetization materials are greatly useful in magnetic recording [1] and permanent magnet industries. Fe-Co alloy is the historically dominant choice for high magnetization, but it is limited by the Slater-Pauling curve [2,3]. $Fe_{16}N_2$ has been reported to have giant saturation magnetization (M_s) beyond the Slater-Pauling limit [4–7], and thus presents a potentially better option. The earth-abundance of the composing elements makes $Fe_{16}N_2$ especially attractive for permanent magnet applications, and promising progress has been made [8–10].

However, due to the difficulties in sample preparation, there are still contradicting results on the M_s of $Fe_{16}N_2$ [11,12]. For thin-film studies, room temperature M_s of 2.8–3.0 T was observed for phase-pure single-crystal $Fe_{16}N_2$ grown by molecular beam epitaxy (MBE) on InGaAs substrate and Fe underlayer [5]. Sun *et al.* also reported high M_s of 2.6–2.9 T in their $Fe_{16}N_2$ films grown by facing target sputtering (FTS) directly on NaCl substrates [13]. Okamoto *et al.* reported high M_s of 2.5 T for α'- and α''-$Fe_{16}N_2$ films with low α''-$Fe_{16}N_2$ fraction prepared by the sputter beam method on GaAs substrate and Fe/Ag underlayer [14]. Ji *et al.* reported M_s of 2.68 T for $Fe_{16}N_2$ films with order parameter 0.4 on GaAs substrate and Fe underlayer, grown by FTS [6].

In addition to the above high-M_s results, there are also reports of nongiant M_s of $Fe_{16}N_2$ below the Slater-Pauling limit. Takahashi *et al.* reported M_s of no more than 2.24 T for their $Fe_{16}N_2$ films grown by FTS on MgO substrate and Fe underlayer [15]. Brewer *et al.* reported M_s of 2.24 T for partially ordered (46%) $Fe_{16}N_2$ films, prepared by reactive sputtering, on Si substrate and Ag underlayer [16]. Yang *et al.* reported M_s of 2.38 T of $Fe_{16}N_2$ films by FTS on MgO substrate and Ag underlayer [17]. M_s of 2.31 T was reported for high-nitrogen-ordered $Fe_{16}N_2$ films grown with FTS on MgO substrate and Cr underlayer [18].

In bulk samples, Huang *et al.* calculated an M_s of 2.66 T for $Fe_{16}N_2$ in a mixture of α'- and α''-$Fe_{16}N_2$, α-Fe, and γ-Fe-N [19]. Coey *et al.* calculated the M_s of $Fe_{16}N_2$ to be 2.1–2.5 T in powder and foil samples containing 40% α''-$Fe_{16}N_2$ [20]. It is more difficult to achieve high M_s in fine particles, and research of $Fe_{16}N_2$ in that direction is more focused on the applications, such as permanent magnets [11,21–24].

There are reports of other interesting magnetic properties of $Fe_{16}N_2$, such as perpendicular magnetic anisotropy and high spin-polarization ratio in thin films [25] and the effect of strain on M_s [26,27]. The Mössbauer spectrum of high-M_s $Fe_{16}N_2$ films grown by MBE showed only one hyperfine field similar to that of α-Fe [28] despite the fact that there are three chemically inequivalent Fe sites in a unit cell. Interestingly, the Mössbauer spectra of low-M_s $Fe_{16}N_2$ films correctly distinguished the three Fe sites by different hyperfine fields [15].

The $Fe_{16}N_2$ crystal has space group $I4/mmm$, and lattice constants $a = 5.72$ Å, $c = 6.29$ Å [29]. N takes the 2*a* Wyckoff position, whereas Fe atoms occupy three different sites. They are 4*e* [Fe(1)], 8*h* [Fe(2)], and 4*d* [Fe(3)], sorted by their distance to a nearest N atom. The crystal structure of $Fe_{16}N_2$ is shown in Fig. 1.

Electronic structure calculations [30–37] often cannot explain the large magnetic moments in $Fe_{16}N_2$. There has been only one experimental report of the magnetic structure of $Fe_{16}N_2$, by neutron powder diffraction [38], but the results are quite different from what we observed in our thin-film samples. In this paper, we report a half-polarized neutron diffraction (HPND) study on $Fe_{16}N_2$ thin films. The magnetic structure of $Fe_{16}N_2$ is solved and compared to theory.

*Author to whom all correspondence should be addressed: jpwang@umn.edu; Also at Department of Chemical Engineering and Materials Science, University of Minnesota, Minneapolis, Minnesota 55455, USA.

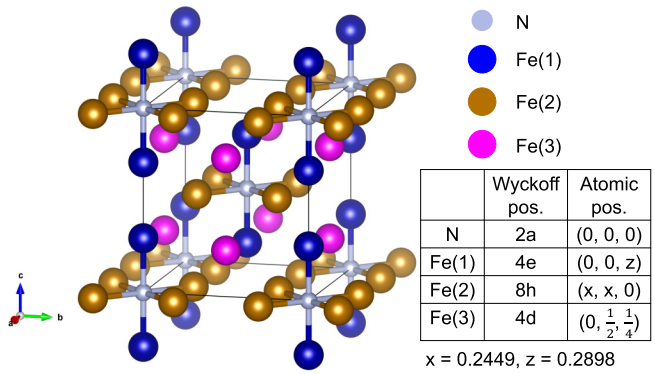

	Wyckoff pos.	Atomic pos.
N	2a	(0, 0, 0)
Fe(1)	4e	(0, 0, z)
Fe(2)	8h	(x, x, 0)
Fe(3)	4d	$(0, \frac{1}{2}, \frac{1}{4})$

FIG. 1. Crystal structure of $Fe_{16}N_2$.

II. EXPERIMENTS AND METHODS

The samples with structure MgO/Cr (10 nm)/$Fe_{16}N_2$ (40 nm)/Cr (10 nm) were deposited using a facing-target sputtering (FTS) system [7], which produces high-quality thin-film samples that are free of radiation damage. The Cr seed layers were deposited at elevated temperature to ensure epitaxial growth. $Fe_{16}N_2$ and Cr capping layers were grown at room temperature. An *in situ* postannealing at 160 °C was performed to all samples to facilitate the transition from α'-Fe_8N to α''-$Fe_{16}N_2$. Through this process, high-quality $Fe_{16}N_2$ films with order parameter between 0.6 and 0.75 were obtained. Details of the deposition method can be found in our previous report [18].

All characterizations were carried out at room temperature. X-ray diffraction (XRD) experiments were performed on a PANalytical X'Pert diffractometer with Cu $K\alpha$ radiation. Cross-sectional transmission electron microscopy (TEM) lamellae were prepared using an FEI Helios NanoLab G4 dual-beam focused ion beam. High-angle annular dark-field scanning TEM (HAADF-STEM) images were acquired on an aberration-corrected FEI Titan G2 60-300 STEM operated at 300 kV with a probe convergence angle of 25 mrad. Conventional TEM images and electron diffraction patterns of the lamellae were acquired on an FEI Technai G2 F30 (S)TEM equipped with a Gatan 4k × 4k Ultrascan charge-coupled device, operated at 300 kV.

HPND experiments were conducted on the triple-axis spectrometer (HB-1) installed at the High-Flux Isotope Reactor (HFIR), Oak Ridge National Laboratory (ORNL). The neutron beam was polarized on a Heusler monochromator. A PG (002) analyzer was used to reduce background noise. The polarization was 0.818 and 0.835 for our two experiments. Samples were saturated by a field of 3 T during measurement. To increase the signal from a thin-film sample, 10 pieces of 1 in.×1 in. samples, each having a $Fe_{16}N_2$ thickness of 40 nm, were stacked together for the measurement. To avoid overlap with powder peaks from the sample holder, Al and Zn sample holders were used for different reflections as appropriate.

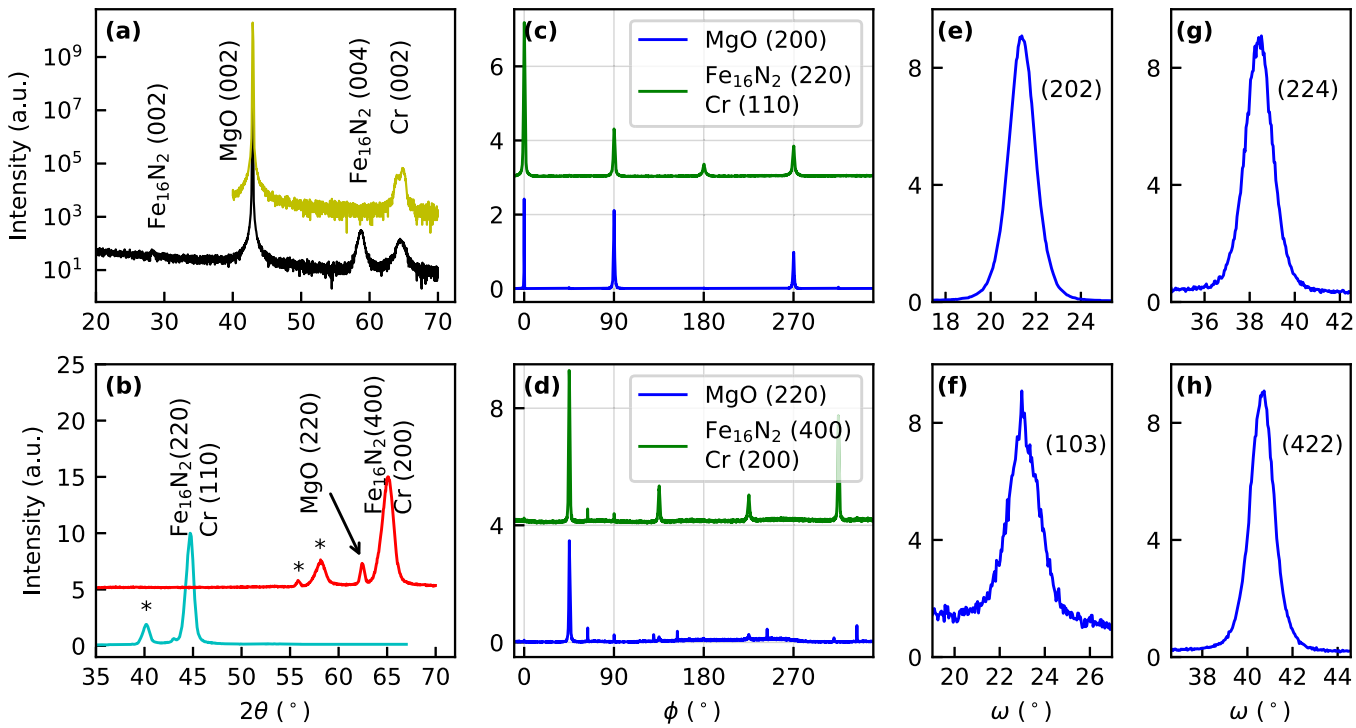

FIG. 2. XRD patterns of a sample with structure MgO/Cr (10 nm)/$Fe_{16}N_2$ (40 nm)/Cr (10 nm). (a) θ-2θ scan with scattering vector along film normal. Also shown is the pattern for a control sample with only Cr seed and capping layers, shifted upward for clarity. (b) In-plane XRD with scattering vector along MgO (200) and (220), respectively. The latter curve is shifted vertically. Peaks labeled * are reflections from Cu $K\beta$ as the in-plane optics is less monochromatized than a typical high-resolution optics. (c) and (d) In-plane ϕ-scans of the $Fe_{16}N_2$ (220) and (400) reflections, respectively. Note that the signal from Cr cannot be separated due to its good lattice match with $Fe_{16}N_2$. The ϕ-scans of the substrate (200) and (220) are also shown in (c) and (d), respectively, to illustrate the epitaxial relation. (e) (202), (f) (103), (g) (224), and (h) (422) are example rocking curves of $Fe_{16}N_2$ (HKL) with $L \neq 0$.

Due to overlapping between $Fe_{16}N_2$ 400 (220) and Cr 200 (110) reflections, control samples with only Cr seed and capping layers were also measured using an unpolarized beam.

The ratio of intensities of the spin-up (polarization parallel to field) and spin-down (polarization antiparallel to field) channels for a Bragg reflection is [39]

$$\frac{I^+}{I^-} = \frac{F_N^2 + F_M^2 + 2PF_NF_M}{F_N^2 + F_M^2 - 2PF_NF_M}, \quad (1)$$

where $F_N = F_N(HKL)$ and $F_M = F_M(HKL)$ are the nuclear and magnetic structure factor for reflection HKL, respectively, and P is the polarization. For both spin channels, we collected rocking curves of $Fe_{16}N_2$ (202), (220), (103), (213), (004), (400), (224), and (422).

III. RESULTS AND DISCUSSION

A. XRD: Epitaxy, crystallinity, and lattice constants

A high-resolution XRD pattern of a $Fe_{16}N_2$ sample is shown in Fig. 2(a), from which it is confirmed that $Fe_{16}N_2$ is textured with (001) out-of-plane orientation. The XRD pattern of a control sample with only Cr seed and capping layers is shown in Fig. 2(a) as the yellow curve. It is observed that there are two Cr (002) peaks slightly separated, indicating different lattice constants of the two Cr layers. This is because the seed layer was deposited at high temperature and epitaxially grown on MgO, which has a 4.2% lattice mismatch with Cr, whereas the capping layer is deposited at room temperature. We also observed that the $Fe_{16}N_2$ (004) peak shifts toward lower angle after postannealing, an indication of strain release during the process. Figure 2(b) shows the θ-2θ scan with scattering vector in-plane. In the lower (upper) curve of Fig. 2(b), the scattering vector is roughly along MgO (200) [MgO (220)]. It can be seen that (in the annealed sample) the substrate peak is well separated from the sample peak due to their lattice mismatch. However, it is impossible to separate Cr peaks from those of $Fe_{16}N_2$ when the reflection has $L = 0$ because of their close lattice constants. Figures 2(c) and 2(d) show in-plane ϕ-scans of $Fe_{16}N_2$ (220) and (400), respectively, with the corresponding ϕ-scans of the MgO substrate shown for reference. The fourfold symmetry can be clearly seen, and it indicates that our $Fe_{16}N_2$ film has perfect in-plane orientation.

TABLE I. XRD θ-2θ scan peak position for $Fe_{16}N_2$ reflections, collected using Cu $K\alpha$ source. (220) and (400) overlap with Cr peaks.

HKL	2θ (deg)	d-spacing (Å)
202	42.82	2.11
220	44.7	2.03
103	46.15	1.97
004	58.75	1.57
400	65.1	1.43
224	76.91	1.24
422	81.26	1.18

In reflections with $L \neq 0$, Cr (cubic) peaks do not interfere with those of $Fe_{16}N_2$ (tetragonal). Example rocking curves of $Fe_{16}N_2$ are shown in Figs. 2(e) (202), 2(f) (103), 2(g) (224), and 2(h) (422). They were collected by rotating the crystal to the appropriate positions determined by the lattice constants of $Fe_{16}N_2$. The various peak positions from θ-2θ scans are tabulated in Table I, from which lattice constants of $Fe_{16}N_2$ were calculated to be $a = 5.71$ Å and $c = 6.28$ Å [40], close to bulk values.

From the XRD results, it is confirmed that our films are epitaxially grown on MgO single-crystal substrate, with the epitaxial relation MgO (001) [110] ∥ Cr (001) [100] ∥ $Fe_{16}N_2$ (001) [100]. After annealing, lattice constants of $Fe_{16}N_2$ relaxed to the bulk values. All grains of $Fe_{16}N_2$ have the same orientation as constrained by epitaxy. So, the film as a whole can be treated as a single crystal in a diffraction experiment.

The rocking curves of a sample with only Cr were analyzed to estimate the grain size. Instrument broadening was corrected by rocking curves of the single-crystalline substrate. Using the Scherrer equation, the grain size is estimated to be 45 nm using Cr (110) and 20 nm using Cr (200). Using the rocking curves of $Fe_{16}N_2$ (220) and (400), the estimated grain size is 17 and 11 nm, respectively. But there is the problem of Cr overlapping, so these values can be used as lower limits.

B. TEM

Overlapping MgO (200), Cr (110), and $Fe_{16}N_2$ (220) diffracted spots were observed in electron diffraction patterns obtained from a cross-sectional TEM lamella (Fig. 3),

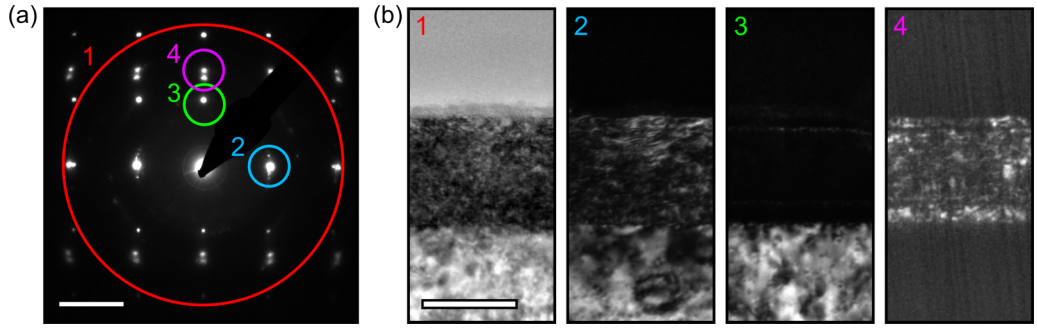

FIG. 3. Electron diffraction and cross-sectional bright-field (BF) and dark-field (DF) TEM imaging. (a) Electron diffraction pattern from a cross-sectional lamella of the film with the substrate aligned to the MgO [010] zone axis. Numbered circles indicate the objective aperture sizes and positions used for imaging. (b) BF- and DF-TEM images obtained with objective apertures shown in (a): 1, BF; 2, DF with the overlapping MgO (200), Cr (110), and $Fe_{16}N_2$ (220) spots; 3, DF with the MgO (002) spot; and 4, DF with the $Fe_{16}N_2$ (004) (inner) and Cr (002) (outer) spots. Scale bars are (a) 5 nm^{-1} and (b) 50 nm.

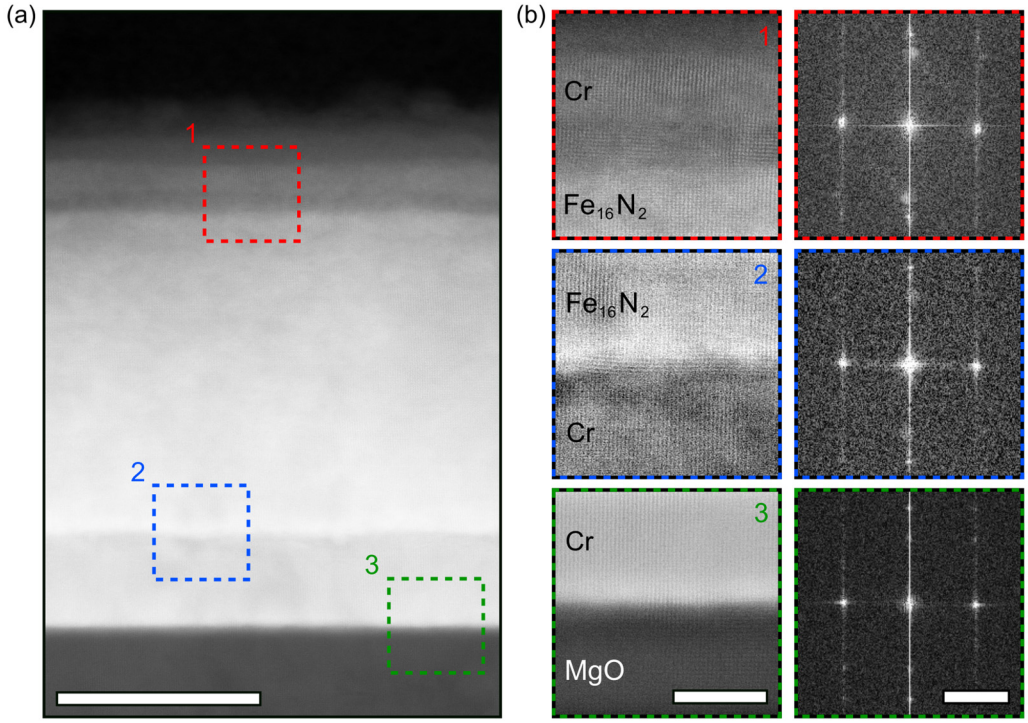

FIG. 4. (a) Cross-sectional HAADF-STEM image of the entire film showing all layers. (b) Atomic-resolution HAADF-STEM images of each interface in the film, obtained from the regions (1–3) indicated in (a), and Fourier transforms of each of these regions, showing the epitaxial relationship between the layers. Each image was individually normalized for visual clarity. The sample was oriented to the [010] zone axis of the MgO substrate. Scale bars are (a) 25 nm; (b) 5 nm and 5 nm^{-1}.

confirming the epitaxial alignment of each layer with the substrate. Faint arcing of each of the Cr and $Fe_{16}N_2$ reflections in the electron diffraction patterns confirms a narrow distribution of low-angle grain boundaries throughout the film.

Atomic-resolution HAADF-STEM images of the film (Fig. 4) show the epitaxial growth of each layer. The grains in the $Fe_{16}N_2$ layer were observed in the HAADF-STEM images to be around 20 nm, with a slight variation in the orientation of each grain around [010] (around the viewing direction).

C. HPND

Using HPND, we collected rocking curves of eight $Fe_{16}N_2$ reflections; they are shown in Fig. 5. In each dataset, spin-up intensity is higher than spin-down. For each reflection, the difference in intensity between the two spin channels is large, indicating that the magnetic structure factor, F_M, is comparable to the nuclear structure factor, F_N, due to the large Fe moments. For low-intensity reflections (103), (213), and (422), the signal is weak compared to the background. For (220) and (400), the respective contributions from Cr (110) and (200) (shown as black curves in the respective subplots of Fig. 5) were approximated by measuring the control samples with an unpolarized beam and subtracted from the total intensity. However, the relative scale of the signals from the two samples is only approximate due to differences in the crystallinity of the Cr capping layer and possibly due to the small difference in sample volume exposed to the neutron beam. For this reason, in the following analysis, only the six reflections with $L \neq 0$—(202), (103), (213), (004), (224), and (422)—are used.

D. Evaluation of existing models of the magnetic structure of $Fe_{16}N_2$

The nuclear and magnetic structure factors are tabulated in Table II. The valence state of Fe in $Fe_{16}N_2$ is unknown. Considering that Fe significantly outnumbers N in this structure, we used the form factor of Fe^0 (zero-valence) [41] for all three Fe sites—Fe(1), Fe(2), and Fe(3)—in the calculation of F_M. However, it should be understood that valence states do have an influence on the magnetic structure solution through magnetic form factors, and that Fe(1) and Fe(2) are likely to have nonzero valence. This effect was studied, and it was found that the best fit to data in Fig. 5 was achieved with Fe^{1+} for Fe(1), Fe^{3+} for Fe(2), and Fe^{1+} for Fe(3), and that the solution is $m_1 = 3.1$, $m_2 = 3.8$, and $m_3 = 1.6$ μ_B. See Sec. III E for details.

Table III summarizes ten magnetic structure models of $Fe_{16}N_2$, nine of which being the results of electronic structure calculations, and the last being from neutron powder diffraction (NPD), along with the present results. The agreement between Ji's model [42] and the present experiment, characterized by a minimum χ^2 error of 3.2, is better than any other model. Notably, the magnetic structure determined by the previous NPD [38] differs so much from the present experimental data that one may wonder if the powder and thin-film samples are actually different materials. The M_s value from

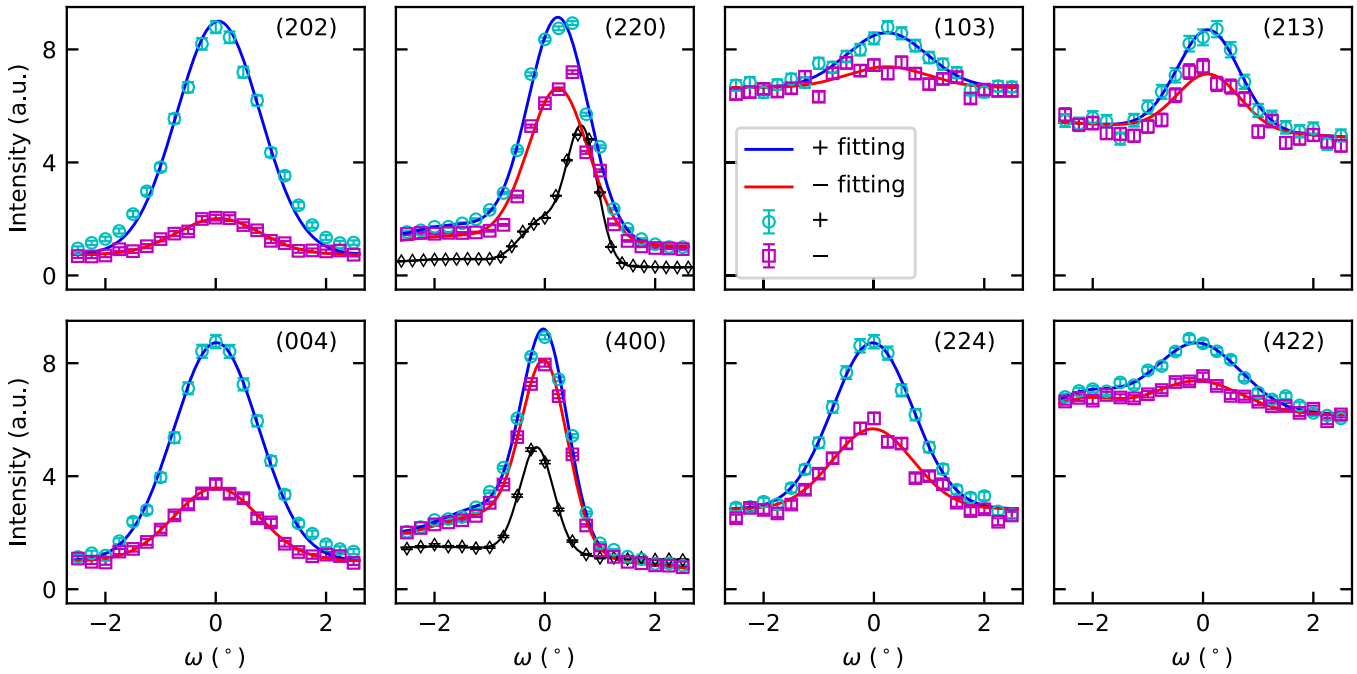

FIG. 5. HPND rocking curves of $Fe_{16}N_2$, collected on 10 pieces of MgO/Cr (10 nm)/$Fe_{16}N_2$ (40 nm)/Cr (10 nm) samples stacked together. For each subplot, the reflection (HKL) is labeled on the graph. Experimental data are plotted as blue open circles for spin up and pink open squares for spin down. Corresponding solid lines are the fitted Gaussian curves. For (220) and (400), rocking curves of the overlapping Cr (110) and (200) are also shown in black, arbitrarily scaled to lower intensity, for the control sample MgO/Cr (10 nm)/Cr (10 nm).

the previous NPD is also so low—only 1370 emu/cm^3—that it looks like an anomaly.

The last two columns of Table III are plotted in Fig. 6(a) [43]. It is interesting to note that models with larger M_s have smaller χ^2 error, thus agreeing better with the present experiment. So, the present experiment supports giant magnetization of $Fe_{16}N_2$. Figure 6(b) shows the experimental I^+/I^- ratio and that from a model calculation. Three theoretical models with the smallest χ^2 error and the experimental NPD model were chosen. The thick solid line, $y = x$, is the ideal case in which a model fits perfectly with the experimental data. It is observed that Ji's model agrees well with the present experiment. All three other models (Sims, Lai, and Hiraka), however, are biased toward one side of the solid line, with two

TABLE II. Parameters used in calculating the magnetic structure of $Fe_{16}N_2$. F_N is calculated using the coherent nuclear scattering lengths $b_{Fe} = 9.45$ fm and $b_N = 9.36$ fm. In the expression of F_M, m_1, m_2, and m_3 are magnetic moments of Fe(1), Fe(2), and Fe(3), respectively, in Bohr magneton. The coefficients in F_M are calculated using the form factors of zero-valence Fe.

HKL	F_N (fm)	F_M (fm)	I^+/I^- expt.
202	−128	$-5.45m_1 - 12.4m_2 - 6.21m_3$	6.46 ± 0.35
103	46.9	$3.93m_1 + 0.369m_2$	2.63 ± 0.43
213	42.1	$3.06m_1 - 0.287m_2$	1.79 ± 0.17
004	153	$2.31m_1 + 8.57m_2 + 4.28m_3$	2.99 ± 0.12
224	152	$1.48m_1 + 5.45m_2 + 2.73m_3$	2.07 ± 0.11
422	−127	$-2.15m_1 - 4.85m_2 - 2.45m_3$	2.13 ± 0.13

TABLE III. Evaluation of the various theoretical and experimental models of the magnetic structure of $Fe_{16}N_2$. M_s is calculated using m_1, m_2, m_3, and bulk lattice constants of $Fe_{16}N_2$. Numbers in parentheses are $4\pi M_s$ in T. The last column is the χ^2 function of a model calculated with the present experimental data and shows how well a model fits into the current experiment. The result of this work is shown in the last row.

Model	m_1 (μ_B)	m_2	m_3	M_s (emu/cm^3)	χ^2
Min [30]	2.13	2.50	2.85	1800 (2.26)	20
Lai [31]	2.36	2.75	3.53	2050 (2.58)	6.6
Huang [32]	2.06	2.42	2.90	1770 (2.22)	22
Sakuma [33]	2.27	2.25	2.83	1730 (2.17)	25
Tanaka [34]	2.17	1.95	2.74	1590 (2.00)	37
Ji [42][a]	3.1	3.25	2.7	2220 (2.79)	3.2
Sims [35][b]	2.83	2.91	3.08	2110 (2.66)	5.1
Ke [36][b]	2.24	2.55	3.12	1890 (2.37)	15
Szymanski [37]	2.74	2.82	2.96	2040 (2.57)	7.4
Hiraka [38]	1.4	1.8	2.6	1370 (1.72)	60
This work[c]	3.1	3.8	1.6	2200 (2.8)	0.75

[a]This work studies the magnetic moment dependence on Hubbard U in the LDA + U calculations. The values used here are those that realize the largest M_s.

[b]Different electronic structure calculation methods were used and compared in this work. The table only lists the one that best fits the present experimental data.

[c]Calculated using the form factors of Fe^{1+}, Fe^{3+}, and Fe^{1+} for Fe(1), Fe(2), and Fe(3), respectively, as this combination minimizes the fitting error. See Sec. III E for details.

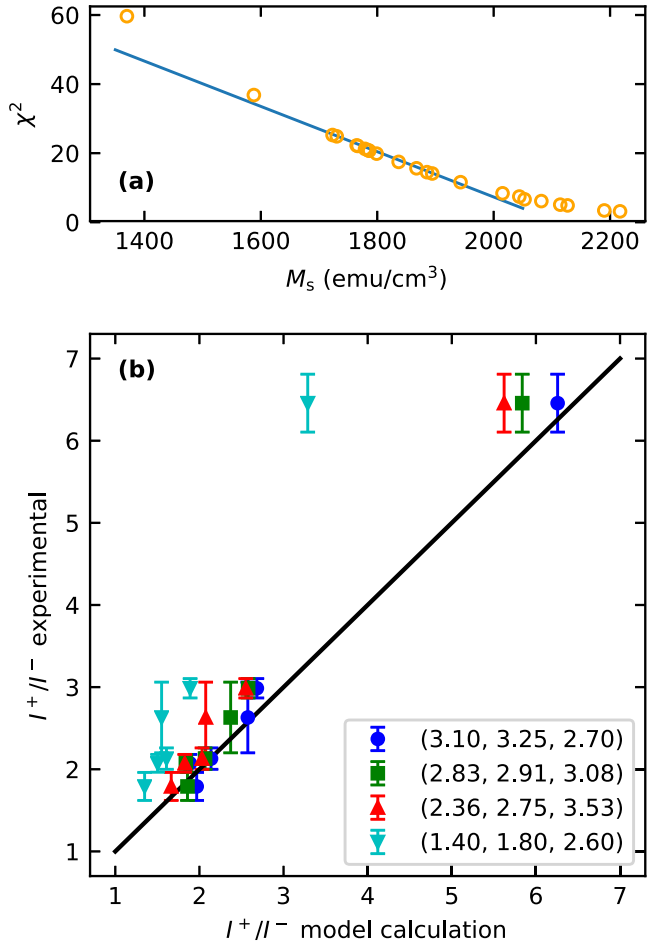

FIG. 6. Evaluation of the magnetic structure models of $Fe_{16}N_2$ against the present experimental results. (a) The χ^2 error of a model vs its M_s, as in the last two columns of Table III. The solid line is a guide to the eye. (b) Plot of the experimental spin-up/spin-down intensity ratio against that calculated from a model. Four models are compared, whose (m_1, m_2, m_3) are labeled; they are the three theoretical models with the smallest χ^2 error (Ji, Sims, and Lai) and one from a previous experiment (Hiraka). Each model has six data points corresponding to the six reflections. The solid line shows $y = x$ and is used to evaluate models.

of them (Lai and Hiraka) having all their data points completely above the line, meaning I^+/I^-(expt.) > I^+/I^-(model) for all six reflections, thus underestimating the magnetic moments.

The success of Ji's model can be understood with the following observation: while in all other models $m_2 < m_3$, his model predicts $m_2 > m_3$. Note from Table II that the coefficient for m_2 is about twice as large as that of m_3 for all even-L reflections (for odd-L reflections, m_3 does not contribute to F_M). So, an increase of moment on Fe(2) results in a larger increase of F_M than that caused by the same amount of moment increase on Fe(3). Also, the atomic ratio of Fe(2) to Fe(3) is 2:1, so an enhanced moment on Fe(2) also increases M_s by twice as much as the same enhancement on Fe(3). In their work, Ji *et al.* studied the magnetic moment evolution with Hubbard U and found that the average moment increases as m_2 increases and m_3 decreases, and that giant M_s only happens at $m_2 > m_3$ [42]. Thus, the present HPND results, together with previous reports of giant M_s of $Fe_{16}N_2$ [4–7], suggest that the true magnetic structure of $Fe_{16}N_2$ might have a larger moment on Fe(2) than previously deemed.

The idea that Fe(2) has a larger moment than Fe(3) is counterintuitive. Whereas the bond length between Fe(1) and Fe(2) is smaller than but close to that of α-Fe, the distance between Fe(3) and Fe(1,2) is considerably larger (see [32] for tabulated bond lengths), so the d-band of Fe(3) can be more localized, giving rise to an enhanced moment. Due to hybridization with the nearest-neighbor N atom, it is expected that Fe(1) and Fe(2) have a lower magnetic moment caused by d-band delocalization. So, intuitively, Fe(3) should have a larger magnetic moment than Fe(1) and Fe(2), which agrees with most theoretical calculations. To explain the large m_2, Ji *et al.* [42] observed that the distorted Fe_6N octahedra, formed by Fe(1), Fe(2), and N atoms, are isolated from each other, as well as from Fe(3). This observation led them to propose that the Fe_6N clusters trap electrons, leading Fe(1) and Fe(2) to have more $3d$ electrons than Fe(3) [42].

This proposal can be tested by using different magnetic form factors for the three different Fe sites because the valence state affects the magnetic form factor. According to Ji, Fe(3) is at a higher valence state. If we use the magnetic form factor of Fe^{2+} for Fe(3), and Fe^0 for Fe(1) and Fe(2), then the χ^2 error of Ji's model will be slightly decreased to 2.8, as compared to 3.2 in Table III. However, the present HPND results alone do not provide sufficient evidence to prove the correctness of Ji's model.

E. Solving the magnetic structure directly

Because the magnetic form factors are different for Fe at different valence states, especially at high momentum transfer Q, and because the valence states of Fe(1), Fe(2), and Fe(3) are unknown, we tried all combinations of valence states from Fe^0 to Fe^{3+} for all three Fe sites and solved the magnetic structure directly from the experimental data using the six reflections and by minimizing the χ^2 error. Selected results with $m_2 < 4.0\ \mu_B$ and $m_3 > 1.0\ \mu_B$ are listed in Table IV. Out of 64 combinations, 5 lead to reasonable solutions, and the average magnetic moment, represented by M_s, is between 2.6 and 2.8 T. Note that in all of these solutions, m_2 is large while m_3 is small. Besides Ji's model [42], it should be noted that N deficiency could also enhance the moment of Fe(2) because it causes the hybridization between N and Fe(2) to be weakened, whereas the average Fe-Fe separation for Fe(2) is still considerably larger than that of α-Fe (see [32] for tabulated bond lengths). In our thin films, N deficiency is likely to exist, especially at the interface, because Cr, having a higher affinity to N than Fe, can extract N atoms from the Fe-N layer during the annealing process.

Finally, we would like to comment on the controversy over M_s of $Fe_{16}N_2$. Using polarized neutron reflectometry, the M_s of these films (MgO substrate and Cr seed layer) was found to be 2.31 T [18], significantly lower than the values in Table IV. However, the density of the film is lower than its nominal value due to the postannealing release of strain, which results in grain boundaries as substantiated by our TEM results. Other studies of $Fe_{16}N_2$ thin films on MgO substrates are likely to

TABLE IV. The effect of magnetic form factors (valence states of Fe) on the magnetic structure solution. For each of Fe(1), Fe(2), and Fe(3), the magnetic form factors of Fe^0, Fe^{1+}, Fe^{2+}, and Fe^{3+} were tried, resulting in 64 combinations in total. The solutions with $m_2 < 4.0\ \mu_B$ and $m_3 > 1.0\ \mu_B$ are shown.

Fe(1)	Fe(2)	Fe(3)	m_1	m_2	m_3	M_s (emu/cm^3)
Fe^0	Fe^{3+}	Fe^{1+}	2.8 ± 0.3	3.8 ± 0.2	1.6 ± 0.5	2200 (2.7)
Fe^{1+}	Fe^{3+}	Fe^0	3.1 ± 0.3	3.9 ± 0.2	1.1 ± 0.4	2200 (2.7)
Fe^{1+}	Fe^{3+}	Fe^{1+}	3.1 ± 0.3	3.8 ± 0.2	1.6 ± 0.5	2200 (2.8)
Fe^{2+}	Fe^{3+}	Fe^{1+}	2.7 ± 0.3	3.8 ± 0.2	1.6 ± 0.5	2200 (2.7)
Fe^{3+}	Fe^{3+}	Fe^{1+}	2.4 ± 0.3	3.7 ± 0.2	1.7 ± 0.5	2100 (2.6)

have the same issue [17,26,44]. Due to interface N diffusion and magnetic dead layers, the M_s value determined from a vibrating sample magnetometer (VSM) is even lower [18]. However, large M_s values that are close to or higher than those in Table IV were reported for $Fe_{16}N_2$ films on GaAs [6,14,27], InGaAs [5], and NaCl [13] substrates. These substrates do not cause tensile strain for epitaxially grown $Fe_{16}N_2$. This further supports our understanding that the relaxation of tensile strain causes an overestimation of sample volume and hence an underestimation of M_s. The only NPD study [38] discussed in Table III and Fig. 6 solved the magnetic structure of $Fe_{16}N_2$ using nanoparticle samples, and the results are quite different from what we observed in the present experiment. As noted by the authors in the NPD study, it may be best to treat thin films and nanoparticles separately, lacking a better understanding of the magnetism of $Fe_{16}N_2$.

IV. CONCLUSIONS

In summary, we performed an HPND study on $Fe_{16}N_2$ thin films at room temperature. XRD and TEM results showed that the orientation of the film was "locked" by the substrate through epitaxy. A postannealing process relaxes strain in the film and promotes a high degree of N ordering. The HPND results suggest that the magnetic moment of Fe(2) is large, and even larger than the moment of Fe(3). This conclusion not only explains why most theoretical magnetic structures underestimate the magnetic structure factors, but also helps understand the origin of giant magnetization in $Fe_{16}N_2$—there are twice as many Fe(2) as there are Fe(3), and a large moment on Fe(2) boosts the average magnetic moment. The local environment of Fe atoms affects the solution to the magnetic structure because the magnetic form factor of Fe depends on its valence state. The saturation magnetization of $Fe_{16}N_2$, calculated from its magnetic structure, is between 2.6 and 2.8 T, regardless of the choice of magnetic form factor.

ACKNOWLEDGMENTS

Parts of this work were carried out in the Characterization Facility, University of Minnesota, which receives partial support from NSF through the MRSEC program DMR-1420013. The HR-TEM study in this work was partially supported by UMN MRSEC program DMR-1420013. This research used resources at the High Flux Isotope Reactor, a DOE Office of Science User Facility operated by the Oak Ridge National Laboratory. The authors thank T. L. Held for her assistance in editing the manuscript.

J.-P.W. has equity and royalty interests in, and serves on the Board of Directors for, Niron Magnetics Inc., a company involved in the commercialization of FeN magnet. The University of Minnesota also has equity and royalty interests in Niron Magnetics Inc. These interests have been reviewed and managed by the University of Minnesota in accordance with its Conflict of Interest policies.

[1] G. Scheunert, O. Heinonen, R. Hardeman, A. Lapicki, M. Gubbins, and R. M. Bowman, A review of high magnetic moment thin films for microscale and nanotechnology applications, Appl. Phys. Rev. **3**, 011301 (2016).

[2] J. C. Slater, Electronic structure of alloys, J. Appl. Phys. **8**, 385 (1937).

[3] L. Pauling, The nature of the interatomic forces in metals, Phys. Rev. **54**, 899 (1938).

[4] T. K. Kim and M. Takahashi, New magnetic material having ultrahigh magnetic moment, Appl. Phys. Lett. **20**, 492 (1972).

[5] Y. Sugita, K. Mitsuoka, M. Komuro, H. Hoshiya, Y. Kozono, and M. Hanazono, Giant magnetic moment and other magnetic properties of epitaxially grown $Fe_{16}N_2$ single-crystal films (invited), J. Appl. Phys. **70**, 5977 (1991).

[6] N. Ji, L. F. Allard, E. Lara-Curzio, and J.-P. Wang, N site ordering effect on partially ordered $Fe_{16}N_2$, Appl. Phys. Lett. **98**, 092506 (2011).

[7] J. P. Wang, N. Ji, X. Liu, Y. Xu, C. Sanchez-Hanke, Y. Wu, F. M. F. de Groot, L. F. Allard, and E. Lara-Curzio, Fabrication of $Fe_{16}N_2$ films by sputtering process and experimental investigation of origin of giant saturation magnetization in $Fe_{16}N_2$, IEEE Trans. Magn. **48**, 1710 (2012).

[8] Y. Jiang, M. A. Mehedi, E. Fu, Y. Wang, L. F. Allard, and J.-P. Wang, Synthesis of $Fe_{16}N_2$ compound free-standing foils with 20 MGOe magnetic energy product by nitrogen ion-implantation, Sci. Rep. **6**, 25436 (2016).

[9] Y. Jiang, V. Dabade, L. F. Allard, E. Lara-Curzio, R. James, and J.-P. Wang, Synthesis of α''-$Fe_{16}N_2$ Compound Anisotropic Magnet by the Strained-Wire Method, Phys. Rev. Appl. **6**, 024013 (2016).

[10] J. Liu, G. Guo, X. Zhang, F. Zhang, B. Ma, and J.-P. Wang, Synthesis of α''-$Fe_{16}N_2$ foils with an ultralow temperature coefficient of coercivity for rare-earth-free magnets, Acta Mater. **184**, 143 (2020).

[11] T. Ogawa, Y. Ogata, R. Gallage, N. Kobayashi, N. Hayashi, Y. Kusano, S. Yamamoto, K. Kohara, M. Doi, M. Takano, and M. Takahashi, Challenge to the synthesis of α''-$Fe_{16}N_2$ compound nanoparticle with high saturation magnetization for rare earth free new permanent magnetic material, Appl. Phys. Express **6**, 073007 (2013).

[12] S. Higashikozono, K. Ito, F. Takata, T. Gushi, K. Toko, and T. Suemasu, Highly oriented epitaxial (α''+α')-$Fe_{16}N_2$ films on α-Fe(001) buffered $MgAl_2O_4$(001) substrates and their magnetization, J. Cryst. Growth **468**, 691 (2017), the 18th International Conference on Crystal Growth and Epitaxy (ICCGE-18).

[13] D. C. Sun, E. Y. Jiang, M. B. Tian, C. Lin, and X. X. Zhang, Epitaxial single crystal $Fe_{16}N_2$ films grown by facing targets sputtering, J. Appl. Phys. **79**, 5440 (1996).

[14] S. Okamoto, O. Kitakami, and Y. Shimada, α''-$Fe_{16}N_2$ phase epitaxially grown by sputter beam method, J. Appl. Phys. **79**, 5250 (1996).

[15] M. Takahashi, H. Shoji, H. Takahashi, H. Nashi, T. Wakiyama, M. Doi, and M. Matsui, Magnetic moment of $\alpha''Fe_{16}N_2$ films (invited), J. Appl. Phys. **76**, 6642 (1994).

[16] M. A. Brewer, C. J. Echer, K. M. Krishnan, T. Kobayashi, and A. Nakanishi, Magnetic and physical microstructure of $Fe_{16}N_2$ films grown epitaxially on Si(001), J. Appl. Phys. **81**, 4128 (1997).

[17] M. Yang, L. F. Allard, N. Ji, X. Zhang, G.-H. Yu, and J.-P. Wang, The effect of strain induced by Ag underlayer on saturation magnetization of partially ordered $Fe_{16}N_2$ thin films, Appl. Phys. Lett. **103**, 242412 (2013).

[18] X. Hang, X. Zhang, B. Ma, V. Lauter, and J.-P. Wang, Epitaxial $Fe_{16}N_2$ thin film on nonmagnetic seed layer, Appl. Phys. Lett. **112**, 192402 (2018).

[19] M. Q. Huang, W. E. Wallace, S. Simizu, A. T. Pedziwiatr, R. T. Obermyer, and S. G. Sankar, Synthesis and characterization of $Fe_{16}N_2$ in bulk form, J. Appl. Phys. **75**, 6574 (1994).

[20] J. M. D. Coey, K. O'Donnell, Q. Qinian, E. Touchais, and K. H. Jack, The magnetization of α'' $Fe_{16}N_2$, J. Phys.: Condens. Matter **6**, L23 (1994).

[21] T. Ogi, A. B. Dani Nandiyanto, Y. Kisakibaru, T. Iwaki, K. Nakamura, and K. Okuyama, Facile synthesis of single-phase spherical α''-$Fe_{16}N_2/Al_2O_3$ core-shell nanoparticles via a gas-phase method, J. Appl. Phys. **113**, 164301 (2013).

[22] C. W. Kartikowati, A. Suhendi, R. Zulhijah, T. Ogi, T. Iwaki, and K. Okuyama, Effect of magnetic field strength on the alignment of α''-$Fe_{16}N_2$ nanoparticle films, Nanoscale **8**, 2648 (2016).

[23] J. Liu, K. Schliep, S.-H. He, B. Ma, Y. Jing, D. J. Flannigan, and J.-P. Wang, Iron nanoparticles with tunable tetragonal structure and magnetic properties, Phys. Rev. Mater. **2**, 054415 (2018).

[24] J. Liu, G. Guo, F. Zhang, Y. Wu, B. Ma, and J.-P. Wang, Synthesis of α''-$Fe_{16}N_2$ ribbons with a porous structure, Nanoscale Adv. **1**, 1337 (2019).

[25] N. Ji, M. S. Osofsky, V. Lauter, L. F. Allard, X. Li, K. L. Jensen, H. Ambaye, E. Lara-Curzio, and J.-P. Wang, Perpendicular magnetic anisotropy and high spin-polarization ratio in epitaxial Fe-N thin films, Phys. Rev. B **84**, 245310 (2011).

[26] N. Ji, V. Lauter, X. Zhang, H. Ambaye, and J.-P. Wang, Strain induced giant magnetism in epitaxial $Fe_{16}N_2$ thin film, Appl. Phys. Lett. **102**, 072411 (2013).

[27] X. Zhang, N. Ji, V. Lauter, H. Ambaye, and J.-P. Wang, Strain effect of multilayer FeN structure on GaAs substrate, J. Appl. Phys. **113**, 17E149 (2013).

[28] Y. Sugita, H. Takahashi, M. Komuro, K. Mitsuoka, and A. Sakuma, Magnetic and Mössbauer studies of single-crystal $Fe_{16}N_2$ and Fe-N martensite films epitaxially grown by molecular beam epitaxy (invited), J. Appl. Phys. **76**, 6637 (1994).

[29] K. H. Jack, The occurrence and the crystal structure of α''-iron nitride; a new type of interstitial alloy formed during the tempering of nitrogen-martensite, Proc. R. Soc. A **208**, 216 (1951).

[30] B. I. Min, Enhancement of Fe magnetic moments in ferromagnetic $Fe_{16}N_2$, Phys. Rev. B **46**, 8232 (1992).

[31] W. Y. Lai, Q. Q. Zheng, and W. Y. Hu, The giant magnetic moment and electronic correlation effect in ferromagnetic nitride $Fe_{16}N_2$, J. Phys.: Condens. Matter **6**, L259 (1994).

[32] M.-Z. Huang and W. Y. Ching, Spin-density distribution in ferromagnetic α''-$Fe_{16}N_2$, Phys. Rev. B **51**, 3222 (1995).

[33] A. Sakuma, Electronic and magnetic structure of iron nitride, $Fe_{16}N_2$ (invited), J. Appl. Phys. **79**, 5570 (1996).

[34] H. Tanaka, H. Harima, T. Yamamoto, H. Katayama-Yoshida, Y. Nakata, and Y. Hirotsu, Electronic band structure and magnetism of $Fe_{16}N_2$ calculated by the FLAPW method, Phys. Rev. B **62**, 15042 (2000).

[35] H. Sims, W. H. Butler, M. Richter, K. Koepernik, E. Şaşıoğlu, C. Friedrich, and S. Blügel, Theoretical investigation into the possibility of very large moments in $Fe_{16}N_2$, Phys. Rev. B **86**, 174422 (2012).

[36] L. Ke, K. D. Belashchenko, M. van Schilfgaarde, T. Kotani, and V. P. Antropov, Effects of alloying and strain on the magnetic properties of $Fe_{16}N_2$, Phys. Rev. B **88**, 024404 (2013).

[37] N. J. Szymanski, V. Adhikari, M. A. Willard, P. Sarin, D. Gall, and S. V. Khare, Prediction of improved magnetization and stability in $Fe_{16}N_2$ through alloying, J. Appl. Phys. **126**, 093903 (2019).

[38] H. Hiraka, K. Ohoyama, Y. Ogata, T. Ogawa, R. Gallage, N. Kobayashi, M. Takahashi, B. Gillon, A. Gukasov, and K. Yamada, Polarized-neutron-diffraction study of the microscopic magnetic structure in $\alpha''-Fe_{16}N_2$ nanoparticles, Phys. Rev. B **90**, 134427 (2014).

[39] G. L. Squires, *Introduction to the Theory of Thermal Neutron Scattering* (Dover, Mineola, NY, 1996), Chap. 9.

[40] We used all reflections in Table I except (220) and (400) because they also come from Cr. If we include them, the results differ by only one part in a thousand.

[41] Coefficients for form factor calculations taken from https://www.ill.eu/sites/ccsl/ffacts/ffactnode5.html.

[42] N. Ji, X. Liu, and J.-P. Wang, Theory of giant saturation magnetization in $\alpha''-Fe_{16}N_2$: Role of partial localization in ferromagnetism of 3d transition metals, New J. Phys. **12**, 063032 (2010).

[43] Results of all methods explored in the works of Sims *et al.* and Ke *et al.* are plotted, whereas only one from each work is shown in Table III.

[44] X. Zhang, M. Yang, Y. Jiang, L. F. Allard, and J.-P. Wang, Thermal stability of partially ordered $Fe_{16}N_2$ film on non-magnetic Ag under layer, J. Appl. Phys. **115**, 17A767 (2014).